Research Article Vol. 10, No. 2 / February 2023 / Optica 255

OPTICA

High-resolution wavefront sensing and aberration analysis of multi-spectral extreme ultraviolet beams

MENGQI DU,[1,*] XIAOMENG LIU,[1,2] ANTONIOS PELEKANIDIS,[1,2] FENGLING ZHANG,[1,2] LARS LOETGERING,[3] PATRICK KONOLD,[4] CHRISTINA L. PORTER,[5] PETER SMORENBURG,[5] KJELD S. E. EIKEMA,[1,2] AND STEFAN WITTE[1,2,6]

[1]ARCNL, Science Park 106, 1098 XG Amsterdam, The Netherlands
[2]LaserLaB, Department of Physics and Astronomy, Vrije Universiteit Amsterdam, De Boelelaan 1105, 1081 HV Amsterdam, The Netherlands
[3]Helmholtz Institut Jena, Frobelstieg 3, 07743 Jena, Germany
[4]Department of Cell and Molecular Biology, Uppsala University, Husargatan 3, 752 37 Uppsala, Sweden
[5]ASML Research, ASML Netherlands B.V., 5504 DR Veldhoven, The Netherlands
[6]e-mail: s.witte@arcnl.nl
*Corresponding author: m.du@arcnl.nl

Received 1 November 2022; revised 9 January 2023; accepted 12 January 2023; published 8 February 2023

Coherent multi-spectral extreme ultraviolet beams have great potential for providing high spatial and temporal resolution for microscopy and spectroscopy applications. But due to the limitations of short-wavelength optics and the broad bandwidth, it remains a challenge to perform quantitative, high-resolution beam characterization. Here we present a wavefront sensing solution based on multiplexed ptychography, with which we show spectrally resolved, high-resolution beam reconstructions. Furthermore, using these high-fidelity quantitative wavefront measurements, we investigate aberration transfer mechanisms in the high-harmonic-generation process, where we present and explain harmonic-order-dependent astigmatism inheritance from the fundamental wavefront. This ptychographic wavefront sensing concept thus enables detailed studies of the high-harmonic-generation process, such as spatiotemporal effects in attosecond pulse formation.

https://doi.org/10.1364/OPTICA.478346

1. INTRODUCTION

Tabletop high-harmonic-generation (HHG) sources produce broadband, spatially coherent radiation in the extreme ultraviolet (XUV) and soft-x-ray (SXR) regimes [1,2]. Recent advances in HHG source development offer high-brightness high-harmonic beams with stable spectrum, intensity, and wavefront distributions, which have enabled a wide range of applications in XUV microscopy [3–5] and attosecond science [6,7]. For many applications, it is beneficial to be able to measure and control the wavefronts of high-harmonic beams to achieve a desired beam shape [8,9], or to improve the focusability [10–12]. Since the energy of HHG pulses has reached the μJ scale, applications in nonlinear optics are actively being pursued, such as XUV-driven multiphoton ionization [13] and attosecond XUV pump–probe spectroscopy [14,15]. These types of experiments have the challenging requirement of accurate control over the focusing properties of attosecond pulses. The large spectral bandwidths of attosecond pulses make them particularly sensitive to spatiotemporal coupling [16], which readily leads to a reduction in focusability, but may also be used as an advantage when accurately controlled [17]. The performance and reproducibility of such experiments critically depend on the ability to characterize and control the focusing properties of broadband XUV radiation, giving rise to a need for high-resolution, spectrally resolved XUV wavefront sensors. Additionally, XUV/SXR sources are under investigation for metrology applications in the semiconductor industry, where focusability is of prime concern since metrology targets are typically small (i.e., <10 um) [18]. Furthermore, certain applications such as model-based profile reconstruction require well-characterized illumination beams to enable reliable matching between simulated and measured diffraction patterns. This necessitates the availability of high-resolution, spectrally resolved beam metrology that can characterize short wavelength beams before and after focusing optics.

Among XUV wavefront sensing methods, Hartmann sensors were first used at a synchrotron source [19], where spectrally filtered monochromatic wavefronts were measured. Spectrally averaged wavefronts of HHG beams have also been characterized in this way [20,21]. Hartmann sensors require only a single-shot measurement, but the spatial resolution is limited by the spacing of the pinhole arrays, which is often in the range of tens or hundreds of micrometers. Point-diffraction interferometry [22] also offers a single-shot measurement of an averaged HHG wavefront by creating a point source as a reference wave. The common limitation of these methods is that any difference between harmonic orders is neglected [20–22].

To characterize wavefronts for each harmonic order, a scanning diffraction method called SWORD has been developed [23,24]. SWORD scans a slit across a high-harmonic beam and records frequency-resolved diffraction signals using a flat-field spectrometer. By calculating the centroid of spectrally separated diffraction orders, local wavefront slopes can be determined for each harmonic independently. Using SWORD, order-dependent intensity and wavefront distributions of high-harmonic beams have been measured and investigated [24]. These measurements led to a better understanding of the physics of the HHG process, e.g., spatiotemporal coupling effects [24]. A similar method termed SCIMITAR [25,26] combines an X-shaped slit with a spectrometer to measure both wavefront and transverse spatial coherence. Both SWORD and SCIMITAR measure the wavefront in consecutive 1D strips, so that a complete beam reconstruction requires either a 2D scan or assumptions on beam symmetry. Furthermore, the spatial resolution is limited by the width of the scanning slit, often in the range of tens of micrometers to maintain practical measurement durations. An alternative method, called lateral shearing interferometry (LSI) [27], circumvents slow scanning by acquiring a double-shot measurement, which, however, relies on producing two identical high-harmonic beams and controlling the shearing between them. Recently, a single-shot spectrally resolved wavefront sensing method called spectroscopic Hartmann sensors was developed [28], where empty apertures in conventional Hartmann masks are replaced by transmission gratings to provide spectral sensitivity. In this case, wavefront reconstructions rely on identification of each diffraction peak from each aperture. This requires the spacing among apertures on the mask to be large, often in the range of tens or hundreds of micrometers, which leads to sparse sampling of the wavefront. That sampling requirement ultimately limits the spatial resolution and accuracy of wavefront reconstructions.

Since many materials absorb XUV and SXR light, refractive optics are impossible, and broadband reflective optics need to be grazing with nm-scale smoothness and figure error. To overcome the optics limitation for this wavelength range, computational methods have been advanced in diffractive optics design for beam control [12,29], as well as in diffractive microscopy [30]. Ptychography [30,31] is a scanning coherent diffractive imaging and wavefront sensing technique, where conventionally, an object is translated across a localized beam in overlapping regions, and a series of diffraction patterns is recorded as a function of scan positions. Using phase-retrieval algorithms, both complex-valued object and probe beams can be reconstructed simultaneously. In the past, ptychography has been explored as a wavefront sensing tool in the optical [32,33] and x-ray regimes [34,35]. The unique advantage of ptychographic wavefront sensing is that it offers robust reconstructions of both intensity profiles and wavefront variations with high spatial resolution given by the numerical aperture of the optical system, which can be orders of magnitude higher than what Hartmann sensors offer, reaching a few and possibly sub-micrometers. Another advantage is that ptychography can be used to measure partially coherent beams, reconstructing multiple spatial and/or temporal modes simultaneously [12,33,35–38]. It has been shown that XUV beams produced from HHG exhibit high spatial coherence [2,39,40], thus being compatible with multi-wavelength ptychography with a single spatial mode per wavelength.

Conventional ptychography uses a focused or spatially localized beam to scan a relatively large, extended object. The finite extent of the beam fulfills the oversampling requirement in the measured diffraction patterns. Our challenge is to directly characterize a free-space propagated, extended multi-spectral high-harmonic beam that is typically much larger than the test object, where different harmonic orders exhibit similar intensity and wavefront distributions. We show that by swapping the roles between the beam and the object, we are able to reconstruct an extended XUV beam, with spectrally resolved intensity and wavefront distributions at a high spatial resolution. We present an optimized design strategy for our ptychographic wavefront sensor (PWFS), capable of characterizing multi-spectral HHG sources. Furthermore, we discuss potential applications of this quantitative, high-fidelity wavefront sensing tool, where it can provide insights into the spatiotemporal coupling, electron trajectories, and other physical aspects of HHG processes. Last but not least, we focus on investigating the aberration transfer mechanism from the fundamental beam to the high-harmonic beam, where we show harmonic-number-dependent beam aberrations. We find a significant effect of the HHG process itself on the wavefront of the harmonics. Combined with theory, we show that the dipole phase can either increase or compensate for astigmatism transferred from an astigmatic fundamental beam.

2. METHODS

A. Experiment

The schematic of the experimental setup is shown in Fig. 1(a). The fundamental near-infrared (NIR) beam is generated from a titanium:sapphire-seeded non-collinear optical parametric chirped-pulse amplifier [41]. The system outputs 4 mJ, 30 fs, 300 Hz NIR pulses centered at 830 nm. A typical spectrum of the fundamental beam is shown in Fig. 1(b). The NIR beam is focused by an $f = 500$ mm lens into an argon gas jet with an aperture size of 200 µm, and a backing pressure of 6 bar. We consider this a loose focusing geometry, where the Rayleigh length of the NIR beam is 5 mm, which is significantly longer than the estimated 1 mm interaction length. The generated harmonic beam is separated from the co-propagating NIR radiation using a 200 nm thick aluminum transmission filter. The high-harmonic spectrum after the filter is obtained by measuring the diffraction from a transmission grating. A typical spectrum is shown in Fig. 1(c), where eight harmonics from the 15th to 29th orders are observed. In contrast to conventional ptychography, where a relatively large object is translated with respect to a localized small beam, in our experiment, we scan a relatively small PWFS across a larger extended multi-spectral XUV beam. In this way, the roles between the probe and the object are exchanged. The PWFS is mounted on an XY translation stage (Smaract, SLC-1730-S-HV) and scanned in a concentric ring pattern. The diffraction patterns are recorded using an XUV-sensitive CCD camera (Andor iKON-L) cooled to −60°C.

B. Binary Mask Design for Ptychographic Wavefront Sensing

To accurately characterize HHG wavefronts, a PWFS mask design is needed that densely samples local wavefront variations, while simultaneously having sufficient spectral diversity. We found that the key elements of a successful binary PWFS design are strongly wavelength-selective elements (gratings) and finite-sized apertures that provide clear near-field diffraction signatures [Fig. 1(d)]. The combination of both far-field and near-field diffractions given by the gratings and apertures ensures robust ptychographic reconstructions. In contrast, tests with PWFS designs that lack one of

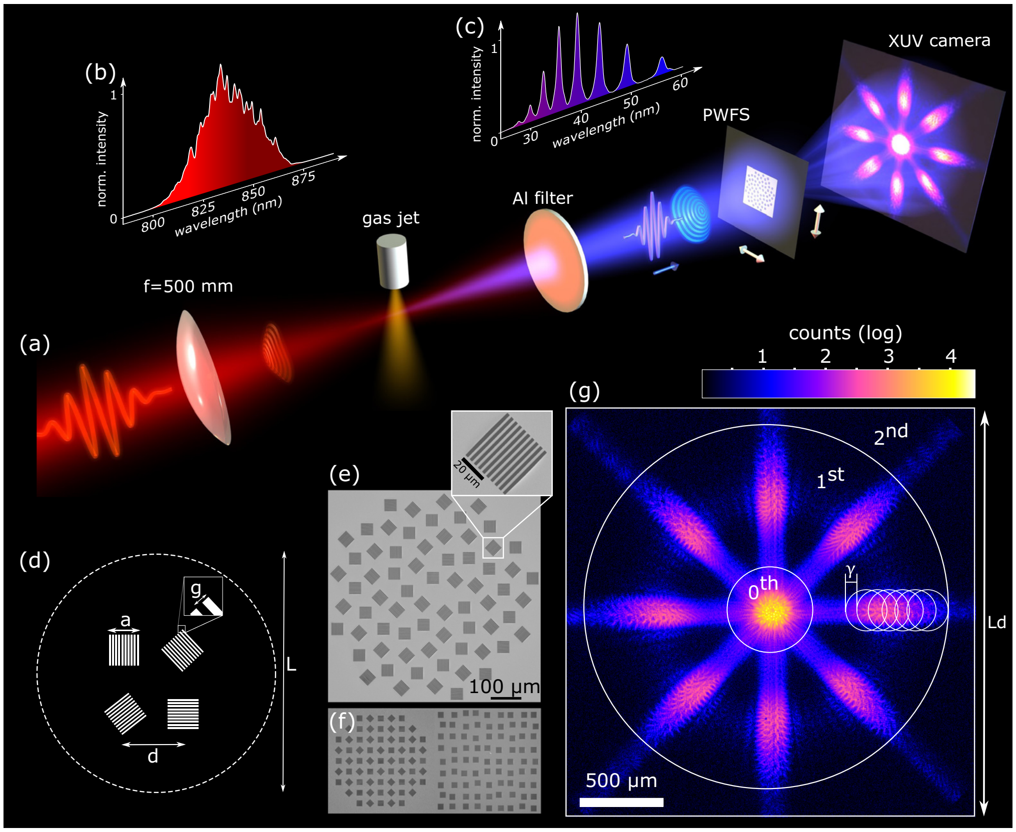

Fig. 1. (a) HHG setup: the NIR beam is focused by a lens $f = 500$ mm into an argon gas jet to generate XUV beams. A 200 nm thick aluminum filter blocks the NIR beam. The PWFS is scanned transversely across the XUV beam, and the diffraction patterns are measured by the XUV camera. (b) Spectrum of the fundamental beam. (c) Spectrum of the high-harmonic beam after the Al filter. (d) Design concept of PWFSs. The key parameters are the aperture size a, grating pitch g, aperture separation distance d, and PWFS size L. (e), (f) SEM images of aperiodic, periodic, and quasi-periodic PWFSs. (g) Example of a measured diffraction pattern from the PWFS in (e).

these features, either containing only large gratings, or consisting of similarly laid-out apertures without gratings, all failed to yield multi-wavelength wavefront reconstructions (see Supplement 1).

To specify a successful PWFS design, we use the Fresnel number $F = \frac{x^2}{\lambda z}$ to quantify the near- and far-field diffraction features, where x is the size of the diffracting element, λ is the XUV wavelength, and z is the camera–PWFS distance. The aperture size a [in Fig. 1(d)] is chosen such that the Fresnel number ($x = a$) of a single aperture is between 0.5 and 5, and the grating pitch g such that its Fresnel number ($x = g$) is <0.1. The average distance d between apertures is 1.5–2 times the aperture size to maintain a relatively high fill factor of about 25%, which allows for efficient use of beam flux. This fill factor is over 2× higher than what can typically be achieved with spectroscopic Hartmann masks [28], as they need larger separation between apertures for reliable spot centroiding. As a result, the efficiency of using PWFSs can be a similar factor two higher given the higher throughput. The grating apertures can be arranged in aperiodic, quasi-periodic, or periodic arrangements [Figs. 1(e) and 1(f)], and different grating orientations can be chosen to increase the camera fill factor.

The binary PWFSs shown in Figs. 1(e) and 1(f) are fabricated using focused-ion-beam milling, where the substrate is a freestanding 100 nm thick silicon nitride membrane, coated with a 100 nm thick gold layer for complete opaqueness in the XUV regime. These PWFSs are designed for measuring our high-harmonic beams in the wavelength range of 20 to 60 nm, with a working distance (PWFS to camera) of 50–80 cm. Each PWFS consists of square apertures with a size of $a = 40$ µm, filled with $g = 4$ µm pitch transmission gratings. The PWFS in Fig. 1(e) contains four different grating orientations, resulting in an eight-fold symmetric diffraction pattern on the camera as shown in Fig. 1(g), where the zeroth and first diffraction orders are fully captured, and the second diffraction orders are partially captured. Note that in our experiments, a complete separation of the first diffraction order maxima from different wavelengths is not required, in contrast to the requirements for spectroscopic Hartmann sensors, which greatly improves transmitted flux. To ensure a sufficient spectral sensitivity, the separation factor γ [in Fig. 1(g)] of the first diffraction orders needs to be more than 25%. The resolution of the wavefront measurement is given by the measured numerical aperture, instead of the spacing between apertures, which can be an order of magnitude higher than using Hartmann sensors.

In a ptychography experiment, the average scan step size needs to be smaller than the aperture size ($a = 40$ µm) to ensure overlap within each aperture during the scan, which in our case is chosen to be 30 µm. A high-overlap factor (above 90%) is generally needed for multi-spectral ptychography [12,37]. In our case, it is 95%. To cover a beam area of 1.5 mm diameter, 800 scan positions are taken. Individual diffraction patterns are recorded at 30 ms exposure time. The reconstructions are performed using the PtyLab [42] software package in Python, optimized for running on a single GPU of a stand-alone computer. Since PtyLab is intended for conventional ptychography with a localized beam, we need to preprocess our data such that our extended beams are treated as the object instead of the probe (see Supplement 1 for more details). More specifically, the ptychographic information multiplexing (PIM) algorithm [37] is used to reconstruct the data, with the input of the diffraction patterns, scan grid, and pre-calibrated harmonic wavelengths. The PWFS design is used as the initial guess for the probe. On average, 50 to 100 iterations are needed to obtain convergence.

3. RESULTS AND DISCUSSION

Eight reconstructed high-harmonic beams at the PWFS plane are shown in Fig. 2(a), where the amplitude and phase are represented by brightness and color, respectively. The spatial resolution of the reconstructed beams is 1.4 µm (full-pitch), over the total field of view of 1.5 mm in diameter. The corresponding reconstructed PWFS is shown in Fig. 2(b), and the inset shows that the 4 µm pitch grating is well resolved. The reconstructions are repeated 10 times with different initial guesses and randomized orders of diffraction patterns. The average of the reconstructed spectral weights is shown in Fig. 2(c) in red, where the error bars show five times the standard deviation. The spectrum in the black dashed line is the wavelength calibration measurement from a transmission grating. The spectral weights reconstructed from ptychography match very well with the grating measurement. From the quantitative beam reconstructions at the PWFS plane, we can propagate them to the camera plane, and incoherently sum up all the harmonic intensities [in Fig. 2(d)]. We compare this calculated beam with the direct bare beam measurement on the camera [in Fig. 2(e)]. Good agreement can be observed, which also verifies the quantitative reconstruction results. Additional quantitative analyses on the spatial resolution, and the reconstruction precision of the high-harmonic wavefronts are included in Supplement 1.

Knowing both the amplitude and phase profiles of high-harmonic beams at the plane of the PWFS enables us to numerically propagate the beams back to the generation plane in the gas jet. Figures 3(a) and 3(b) show beam cross sections as a function of propagation distance in the xz (horizontal) and yz (vertical) planes, respectively, where the red lines indicate the gas jet position. The divergence and focal positions of each harmonic beam can clearly be identified, and a comparison of the x and y cross sections reveals significant astigmatism in the HHG beams. In the x direction, all harmonic beams focus at a similar distance. Except for the longest wavelength, all beams exhibit virtual foci upstream of the gas jet. In contrast, in the y direction, a clear difference of focus positions with respect to the gas jet can be observed, and these are real foci because they appear downstream of the gas jet. This wavelength-dependent focus variation is effectively an intrinsic chromatic aberration of the HHG process, and this effect has recently attracted attention from the attosecond community [10,16,24]. Our PWFS approach has sufficient resolution to quantify this effect, enabling an accurate study of the influence of the dipole phase as a function of the generation geometry.

Propagating all harmonic beams to a common focal plane enables us to investigate the spatiospectral and spatiotemporal properties of the XUV beam focus. Figure 4(a) displays the intensity distributions of each harmonic focus. The beam waist (2σ) of the harmonic beam is on average 20 µm, and the Rayleigh length is about 3 cm. The incoherent addition of all harmonic foci gives the polychromatic focus of attosecond pulses in Fig. 4(b). The broadband focus has a beam waist of 40 µm. We can see that the upper and lower parts of the beam are not reached by all harmonics, in contrast to the beam center where all harmonics are present.

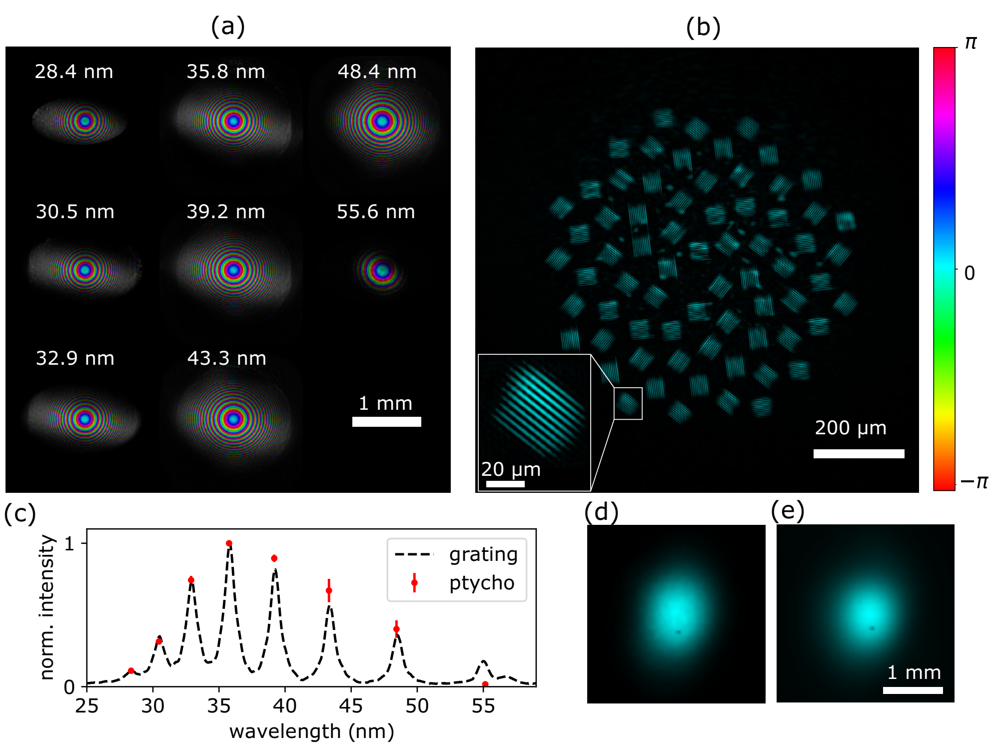

Fig. 2. Ptychographic reconstruction of (a) eight harmonic beams and (b) PWFS mask. In these images, brightness represents amplitude and color represents phase. (c) Retrieved spectral weights, average of 10 independent reconstructions. The error bars show 5× the standard deviation. Images of the XUV beam at the camera plane (d) calculated from the reconstructions and (e) directly measured by the camera.

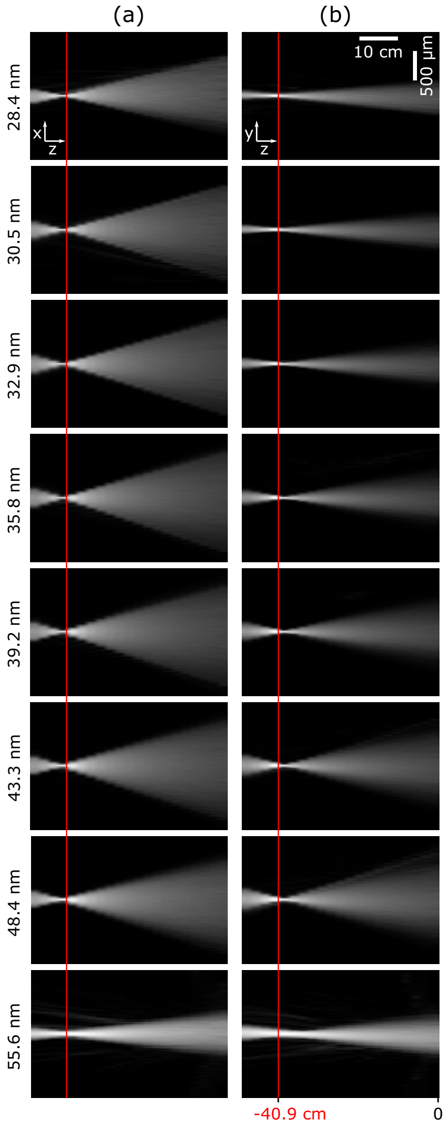

Fig. 3. Cross section of eight high-harmonic beams in (a) xz and (b) yz planes. Beams propagate from left to right. The red lines indicate the physical location of the gas jet. The right edge of the images is the plane where the PWFS is located.

Within this focal distribution, three separate locations are marked with colored dots: the retrieved spectra at these positions [Fig. 4(c)] show significant differences. From these spectra, the local Fourier-limited temporal pulse shapes can be determined [Fig. 4(d)], the full-widths-at-half-maxima (FWHMs) of which are 180, 215, and 246 as. To highlight the complicated spatiotemporal couplings that can arise from such spectrally dependent wavefronts, a spatial map of the Fourier-limited pulse duration at the focus is shown in Fig. 4(e), and the duration varies between 150 and 280 as.

Figure 3(a) also shows another important aspect of the focusing properties of attosecond XUV pulses, namely, the wavelength-dependent astigmatism in high-harmonic beams. Previous studies [20,21,43] have investigated how aberrations are transferred from fundamental to high-harmonic beams. However, only spectrally averaged wavefront measurements with limited spatial resolutions have been reported. Our spectrally resolved, high-resolution wavefront reconstructions enable a more complete and quantitative analysis. To quantify the wavefront transfer in the HHG process, high-resolution measurements of the fundamental beam wavefront are performed using ptychography in parallel to the XUV measurements (see Supplement 1 for details).

We analyze beam aberrations using Zernike decomposition, where each wavefront is decomposed into mutually orthogonal Zernike polynomials with their resulting coefficients. We vary the astigmatism in the fundamental beam by tilting the focusing lens before the gas jet. Figure 5 displays two sets of data with more and less aberrated beams (with a lent tilt of 8.1°) in the top and bottom rows, respectively. The reconstructed fundamental beams are propagated to the equivalent gas jet location, where the Zernike coefficients are extracted as presented in Figs. 5(a) and 5(d). To better visualize higher-order aberrations in the generated high-harmonic beams, the first four Zernike components in Noll convention [44], i.e., piston, tip, tilt, and defocus, are excluded in Figs. 5(b) and 5(e). The corresponding Zernike coefficients for higher-order polynomials (Noll index > 4) are plotted in Figs. 5(c) and 5(f). First, we observe that aberrations, more specifically, the oblique and vertical astigmatism contained in the fundamental beam, are transferred to the high-harmonic wavefronts. Second, harmonic-order-dependent aberrations can also be seen in the aberrated case, in the sense that some harmonic orders inherit more astigmatism from the fundamental wavefront than others. This variation can be explained by taking into account the dipole phase

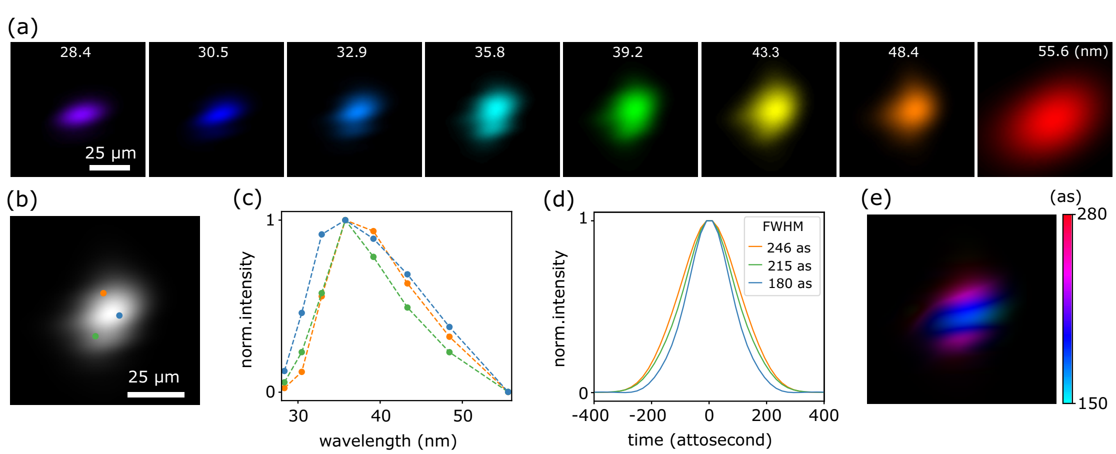

Fig. 4. (a) Color coded intensity plots of each harmonic focus. (b) Intensity profile of the polychromatic focus summed over all high-harmonic beams. (c) Spectra and (d) Fourier-limited pulses, at three different locations within the focus as marked in (b). (e) 2D spatiotemporal map of the polychromatic focus.

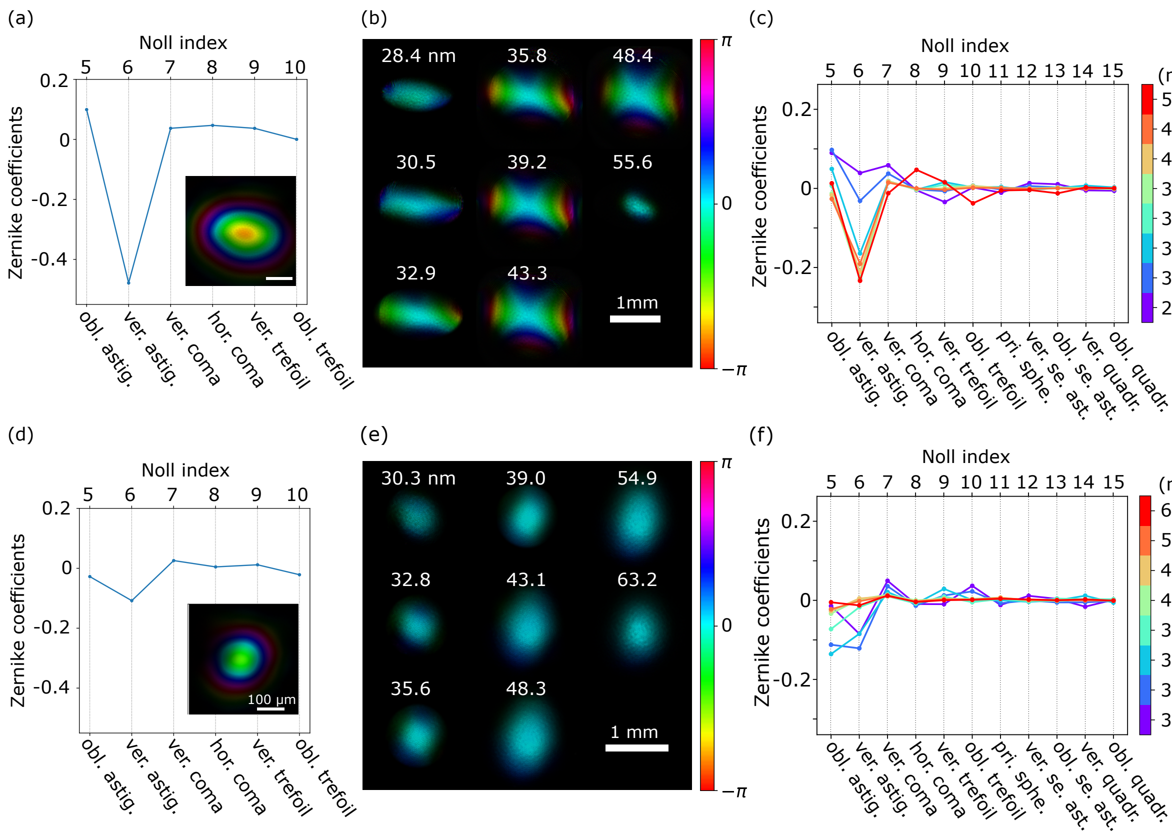

Fig. 5. (a)–(c) Aberrated fundamental beam, high-harmonic beams, and their Zernike coefficients and (d)–(f) aberration-minimized fundamental beam, high-harmonic beams, and their Zernike coefficients, respectively. The chosen pupil diameter for Zernike fits of harmonic beams is 6.3 mm.

contribution in the HHG process. Following an analytical solution to the time-dependent Schrödinger equation describing the single-atom response in HHG [16], the wavefront of a q th-order harmonic beam can be expressed with two contributions:

$$\Phi_q = q\Phi_f + \Phi_d(I_f), \tag{1}$$

where the first term describes the direct phase transfer from the phase of the fundamental beam (Φ_f) to the qth harmonic, and the second term is the dipole phase contribution ($\Phi_d(I_f)$), resulting from the electron propagation in the continuum. Generally, two different electron trajectories, i.e., long and short trajectories, have different dipole phases. Since in our current experiments, the phase matching condition favors short trajectories, in the discussion below, only the dipole phase for short trajectories is considered. Following an analytical solution to the strong-field approximation, the dipole phase is expressed as $\Phi_d(I_f) = \gamma_s(\Omega_q - \Omega_p)^2/I_f$ [16], where γ_s is a constant related to the central wavelength of the drive laser, Ω_q is the frequency of the qth harmonic, Ω_p is the frequency related to the ionization energy of the gas $E_{\text{gas}} = \hbar\Omega_p$, and I_f is the fundamental intensity. Therefore, the high-harmonic wavefront is affected by both the fundamental phase and intensity, as well as the harmonic order. In addition, the order-dependent intensity distributions in the far field that we resolved from ptychography measurements are also interesting [see Fig. 2(a) and Fig. 5]. While a purely astigmatic beam in the far field is in itself not elliptical, the astigmatic driving beam at the gas jet plane can be [see Fig. 5(a)], as it is near the focus. Such an elliptical intensity distribution will lead to an elliptical HHG intensity profile as well, as the intensity governs conversion efficiency. Therefore, an astigmatic driving beam can lead to an elliptical or round HHG intensity profile, depending on the position of the gas jet.

We can now use this insight to study and control the astigmatism in high-harmonic beams, by tuning the dipole phase effect through a variation of the fundamental intensity profile. To demonstrate this concept, we generate high-harmonic beams from two different gas jet positions with respect to the beam waist of the astigmatic fundamental beam, as shown in Fig. 6. The cross-section (xz and yz) plot shows that the two foci of the fundamental beam are separated by 15 mm, and the focus in the x axis is upstream of the one in y. In scenario 1, the gas jet is placed at position 1 in between the two foci, where the fundamental intensity is circularly symmetric. The phase and intensity profiles of the fundamental beam are displayed in Fig. 6(a). From the direct phase transfer ($q\Phi_f$), high-harmonic beams inherit the astigmatism from the fundamental phase. The circular fundamental intensity leads to a stigmatic, or circularly symmetric dipole phase contribution. The resulting HHG wavefront aberrations are therefore dominated by the direct phase transfer, and higher-order harmonics exhibit larger Zernike coefficients for astigmatism [Fig. 6(b)].

In scenario 2, the astigmatism contribution induced by the dipole phase and fundamental wavefront partially compensate for each other. Specifically, the gas jet is moved to position 2, which is closer to the vertical focus, and therefore the intensity profile of the fundamental beam is more elliptical [in Fig. 6(d)]. This non-circular intensity shape results in an astigmatic dipole phase contribution. Intuitively, since the dipole phase ($\propto I_f^{-1}$) is always divergent, this elliptical profile will lead to a stronger wavefront

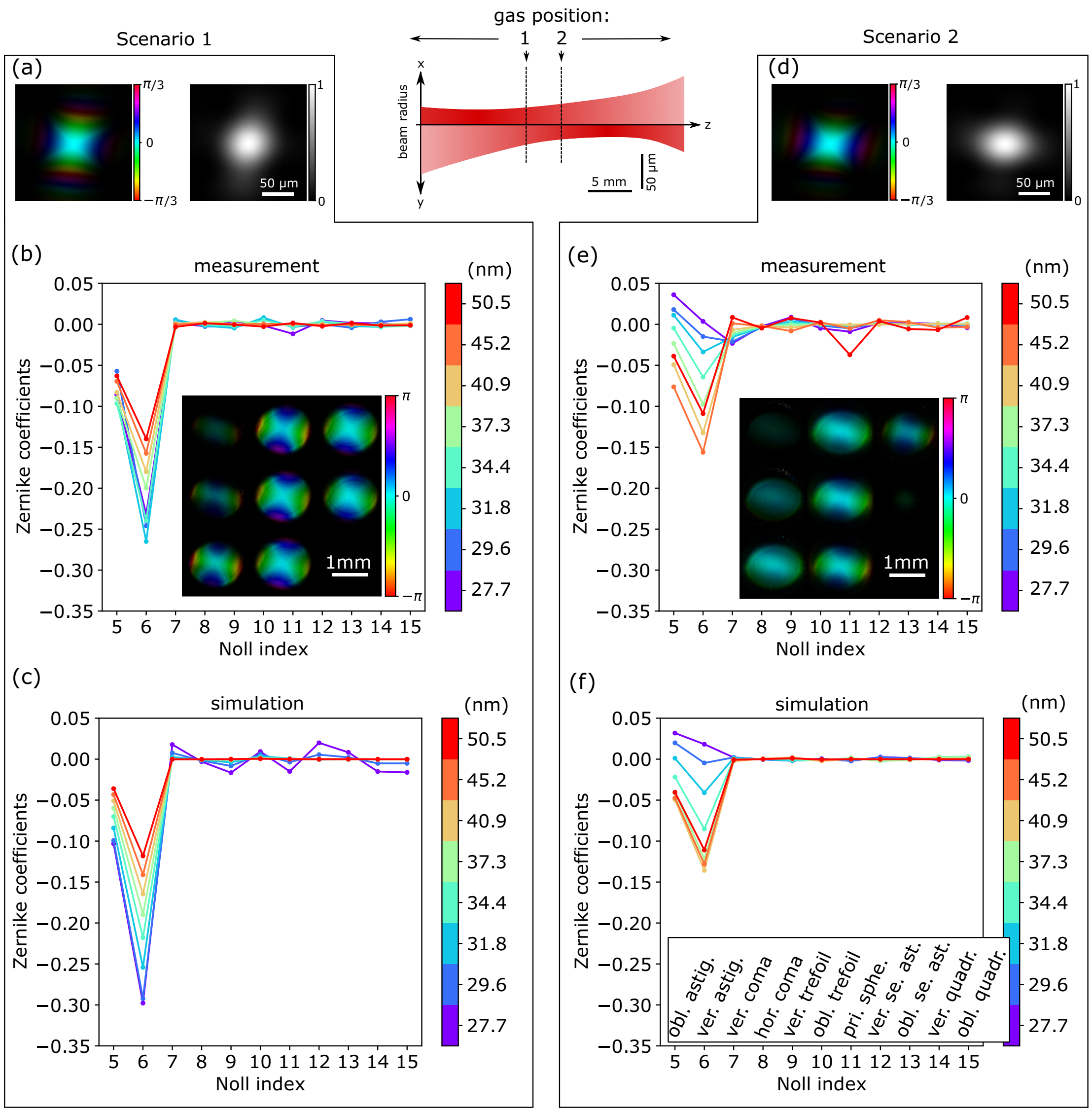

Fig. 6. Astigmatism transfer analysis on HHG beams generated at two gas positions. (a) Fundamental phase and intensity, (b), (c) Zernike coefficients of measured and simulated HHG beams in scenario 1 (gas position 1). (d) Fundamental phase and intensity, (e), (f) Zernike coefficients of measured and simulated HHG beams in scenario 2 (gas position 2). The chosen pupil diameter for Zernike fits in (b), (c) is 6.6 mm.

curvature in the vertical direction, while the wavefront of the fundamental at position 2 is more divergent in the x direction. Consequently, the two foci will shift closer to each other, and the dipole phase results in significant astigmatism compensation. Our measurements shown in Fig. 6(e) indeed confirm that fewer astigmatic high-harmonic beams are generated in this case. Moreover, the dipole phase has a quadratic dependence on the harmonic order; hence, the compensation effect is stronger for higher harmonics, which is indeed what we observe in Fig. 6(e). Taking a single harmonic beam at 31.8 nm as an example, the focus shift in x and y directions is 42 mm in scenario 1, while only 5 mm in scenario 2. To substantiate our findings, we simulated the high-harmonic wavefronts (details in Supplement 1) in these two scenarios using the theoretical model [Eq. (1)], where we input the measured fundamental intensity and phase [Figs. 6(a) and 6(d)]. The Zernike analysis on the simulated HHG wavefronts [Figs. 6(c) and 6(f)] shows good agreement with our experimental data.

4. CONCLUSION

We presented a high-resolution ptychographic wavefront sensing method for multi-spectral, spatially extended high-harmonic sources. The best design strategy for a PWFS is discussed, and high-fidelity reconstructions of eight harmonic beams with a full-pitch spatial resolution of 1.4 μm are shown. Using the quantitative reconstruction results and numerical propagation, we evaluated the spatiospectral, as well as spatiotemporal focusing properties of HHG pulses. Furthermore, we studied the aberration transfer mechanism in the HHG process, where we observe a strong correlation in astigmatism between fundamental and high-harmonic beams. Moreover, with the help of a theoretical model, we experimentally demonstrated that it is possible to control the astigmatism in the high-harmonic wavefronts generated from an astigmatic fundamental beam by tuning the dipole phase contribution through optimizing the gas jet position.

We believe that ptychographic wavefront metrology has great potential to facilitate quantitative studies on HHG and attosecond

XUV pulses at unprecedented spatial and spectral resolution. As an outlook, by combining a systematic focus scan with wavefront measurements, we can further investigate chromatic aberration in the XUV beam to uncover potential spatiotemporal couplings in attosecond pulses. Moreover, using adaptive optics to precisely control and manipulate various aberration forms besides astigmatism in the fundamental beam will enable us to study more complicated aberration transfer mechanisms in the HHG process, which may in turn facilitate wavefront shaping methods for XUV beams.

Funding. Nederlandse Organisatie voor Wetenschappelijk Onderzoek (H2020 EC-GA 871124); European Research Council (ERC-CoG 864016).

Disclosures. The authors declare no conflicts of interest.

Data availability. Data underlying the results presented in this paper are not publicly available at this time but may be obtained from the authors upon reasonable request.

Supplemental document. See Supplement 1 for supporting content.

REFERENCES

1. M. Ferray, A. L'Huillier, X. F. Li, L. A. Lompre, G. Mainfray, and C. Manus, "Multiple-harmonic conversion of 1064 nm radiation in rare gases," J. Phys. B **21**, L31–L35 (1988).
2. R. Bartels, A. Paul, H. Green, H. Kapteyn, M. Murnane, S. Backus, I. Christov, Y. Liu, D. Attwood, and C. Jacobsen, "Generation of spatially coherent light at extreme ultraviolet wavelengths," Science **297**, 376–378 (2002).
3. M. Zürch, J. Rothhardt, S. Hädrich, S. Demmler, M. Krebs, J. Limpert, A. Tünnermann, A. Guggenmos, U. Kleineberg, and C. Spielmann, "Real-time and sub-wavelength ultrafast coherent diffraction imaging in the extreme ultraviolet," Sci. Rep. **4**, 7356 (2014).
4. E. R. Shanblatt, C. L. Porter, D. F. Gardner, G. F. Mancini, R. M. Karl, M. D. Tanksalvala, C. S. Bevis, V. H. Vartanian, H. C. Kapteyn, D. E. Adams, and M. M. Murnane, "Quantitative chemically specific coherent diffractive imaging of reactions at buried interfaces with few nanometer precision," Nano Lett. **16**, 5444–5450 (2016).
5. M. Tanksalvala, C. L. Porter, Y. Esashi, B. Wang, N. W. Jenkins, Z. Zhang, G. P. Miley, J. L. Knobloch, B. McBennett, N. Horiguchi, S. Yazdi, J. Zhou, M. N. Jacobs, C. S. Bevis, R. M. Karl, P. Johnsen, D. Ren, L. Waller, D. E. Adams, S. L. Cousin, C.-T. Liao, J. Miao, M. Gerrity, H. C. Kapteyn, and M. M. Murnane, "Nondestructive, high-resolution, chemically specific 3D nanostructure characterization using phase-sensitive EUV imaging reflectometry," Sci. Adv. **7**, eabd9667 (2021).
6. P. Á. Corkum and F. Krausz, "Attosecond science," Nat. Phys. **3**, 381–387 (2007).
7. J. Li, J. Lu, A. Chew, S. Han, J. Li, Y. Wu, H. Wang, S. Ghimire, and Z. Chang, "Attosecond science based on high harmonic generation from gases and solids," Nat. Commun. **11**, 2748 (2020).
8. F. Sanson, A. K. Pandey, I. Papagiannouli, F. Harms, G. Dovillaire, E. Baynard, J. Demailly, O. Guilbaud, B. Lucas, O. Neveu, M. Pittman, D. Ros, M. Richardson, E. Johnson, W. Li, P. Balcou, and S. Kazamias, "Highly multimodal structure of high topological charge extreme ultraviolet vortex beams," Opt. Lett. **45**, 4790–4793 (2020).
9. A. K. Pandey, A. de las Heras, T. Larrieu, J. S. Román, J. Serrano, L. Plaja, E. Baynard, M. Pittman, G. Dovillaire, S. Kazamias, C. Hernández-García, and O. Guilbaud, "Characterization of extreme ultraviolet vortex beams with a very high topological charge," ACS Photon. **9**, 944–951 (2022).
10. L. Quintard, V. Strelkov, J. Vabek, O. Hort, A. Dubrouil, D. Descamps, F. Burgy, C. Péjot, E. Mével, F. Catoire, and E. Constant, "Optics-less focusing of XUV high-order harmonics," Sci. Adv. **5**, eaau7175 (2019).
11. M. Hoflund, J. Peschel, M. Plach, H. Dacasa, K. Veyrinas, E. Constant, P. Smorenburg, H. Wikmark, S. Maclot, C. Guo, C. Arnold, A. L'Huillier, and P. Eng-Johnsson, "Focusing properties of high-order harmonics," Ultrafast Sci. **2021**, 9797453 (2021).
12. L. Loetgering, X. Liu, A. C. C. D. Beurs, M. Du, G. Kuijper, K. S. E. Eikema, and S. Witte, "Tailoring spatial entropy in extreme ultraviolet focused beams for multispectral ptychography," Optica **8**, 130–138 (2021).
13. B. Major, O. Ghafur, K. Kovács, K. Varjú, V. Tosa, M. J. J. Vrakking, and B. Schütte, "Compact intense extreme-ultraviolet source," Optica **8**, 960–965 (2021).
14. Y. Nabekawa, T. Shimizu, T. Okino, K. Furusawa, H. Hasegawa, K. Yamanouchi, and K. Midorikawa, "Conclusive evidence of an attosecond pulse train observed with the mode-resolved autocorrelation technique," Phys. Rev. Lett. **96**, 083901 (2006).
15. P. Tzallas, D. Charalambidis, N. A. Papadogiannis, K. Witte, and G. D. Tsakiris, "Direct observation of attosecond light bunching," Nature **426**, 267–271 (2003).
16. H. Wikmark, C. Guo, J. Vogelsang, P. W. Smorenburg, H. Coudert-Alteirac, J. Lahl, J. Peschel, P. Rudawski, H. Dacasa, S. Carlström, S. Maclot, M. B. Gaarde, P. Johnsson, C. L. Arnold, and A. L'Huillier, "Spatiotemporal coupling of attosecond pulses," Proc. Natl. Acad. Sci. USA **116**, 4779–4787 (2019).
17. H. Vincenti and F. Quéré, "Attosecond lighthouses: how to use spatiotemporally coupled light fields to generate isolated attosecond pulses," Phys. Rev. Lett. **108**, 113904 (2012).
18. C. Porter, T. Coenen, N. Geypen, S. Roobol, S. Scholz, L. van Rijswijk, H.-K. Nienhuys, J. Reinink, J. Ploegmakers, O. Gawhary, P. Helfenstein, J. Bogdanowicz, H. Mertens, A.-H. Tamaddon, and A.-L. Charley, "Soft x-ray scatterometry: at-resolution, 3D metrology for the EUV era," in *FCMN Conference* (2022), pp. 93–95.
19. P. Mercère, P. Zeitoun, M. Idir, S. L. Pape, D. Douillet, X. Levecq, G. Dovillaire, S. Bucourt, K. A. Goldberg, P. P. Naulleau, and S. Rekawa, "Hartmann wave-front measurement at 13.4 nm with $\lambda_{EUV}/120$ accuracy," Opt. Lett. **28**, 1534–1536 (2003).
20. C. Valentin, J. Gautier, J.-P. Goddet, C. Hauri, T. Marchenko, E. Papalazarou, G. Rey, S. Sebban, O. Scrick, P. Zeitoun, G. Dovillaire, X. Levecq, S. Bucourt, and M. Fajardo, "High-order harmonic wave fronts generated with controlled astigmatic infrared laser," J. Opt. Soc. Am. B **25**, B161–B166 (2008).
21. H. Dacasa, H. Coudert-Alteirac, C. Guo, E. Kueny, F. Campi, J. Lahl, J. Peschel, H. Wikmark, B. Major, E. Malm, D. Alj, K. Varjú, C. L. Arnold, G. Dovillaire, P. Johnsson, A. L'Huillier, S. Maclot, P. Rudawski, and P. Zeitoun, "Single-shot extreme-ultraviolet wavefront measurements of high-order harmonics," Opt. Express **27**, 2656–2670 (2019).
22. D. G. Lee, J. J. Park, J. H. Sung, and C. H. Nam, "Wave-front phase measurements of high-order harmonic beams by use of point-diffraction interferometry," Opt. Lett. **28**, 480–482 (2003).
23. E. Frumker, G. G. Paulus, H. Niikura, D. M. Villeneuve, and P. B. Corkum, "Frequency-resolved high-harmonic wavefront characterization," Opt. Lett. **34**, 3026–3028 (2009).
24. E. Frumker, G. G. Paulus, H. Niikura, A. Naumov, D. M. Villeneuve, and P. B. Corkum, "Order-dependent structure of high harmonic wavefronts," Opt. Express **20**, 13870–13877 (2012).
25. D. T. Lloyd, K. O'Keeffe, and S. M. Hooker, "Complete spatial characterization of an optical wavefront using a variable-separation pinhole pair," Opt. Lett. **38**, 1173–1175 (2013).
26. D. T. Lloyd, K. O'Keeffe, P. N. Anderson, and S. M. Hooker, "Gaussian-Schell analysis of the transverse spatial properties of high-harmonic beams," Sci. Rep. **6**, 30504 (2016).
27. D. R. Austin, T. Witting, C. A. Arrell, F. Frank, A. S. Wyatt, J. P. Marangos, J. W. Tisch, and I. A. Walmsley, "Lateral shearing interferometry of high-harmonic wavefronts," Opt. Lett. **36**, 1746–1748 (2011).
28. L. Freisem, G. S. M. Jansen, D. Rudolf, K. S. E. Eikema, and S. Witte, "Spectrally resolved single-shot wavefront sensing of broadband high-harmonic sources," Opt. Express **26**, 6860–6871 (2018).
29. L. Loetgering, M. Baluktsian, K. Keskinbora, R. Horstmeyer, T. Wilhein, G. Schütz, K. S. E. Eikema, and S. Witte, "Generation and characterization of focused helical x-ray beams," Sci. Adv. **6**, eaax8836 (2020).
30. P. Thibault, M. Dierolf, A. Menzel, O. Bunk, C. David, and F. Pfeiffer, "High-resolution scanning x-ray diffraction microscopy," Science **321**, 379–382 (2008).
31. J. M. Rodenburg and H. M. L. Faulkner, "A phase retrieval algorithm for shifting illumination," Appl. Phys. Lett. **85**, 4795–4797 (2004).
32. M. Du, L. Loetgering, K. S. E. Eikema, and S. Witte, "Measuring laser beam quality, wavefronts, and lens aberrations using ptychography," Opt. Express **28**, 5022–5034 (2020).
33. D. Goldberger, D. Schmidt, J. Barolak, B. Ivanic, C. G. Durfee, and D. E. Adams, "Spatiospectral characterization of ultrafast pulse-beams by multiplexed broadband ptychography," Opt. Express **29**, 32474–32490 (2021).

34. C. M. Kewish, M. Guizar-Sicairos, C. Liu, J. Qian, B. Shi, C. Benson, A. M. Khounsary, J. Vila-Comamala, O. Bunk, J. R. Fienup, A. T. Macrander, and L. Assoufid, “Reconstruction of an astigmatic hard x-ray beam and alignment of k-b mirrors from ptychographic coherent diffraction data,” Opt. Express **18**, 23420–23427 (2010).
35. B. J. Daurer, S. Sala, M. F. Hantke, H. K. N. Reddy, J. Bielecki, Z. Shen, C. Nettelblad, M. Svenda, T. Ekeberg, G. A. Carini, P. Hart, T. Osipov, A. Aquila, N. D. Loh, F. R. N. C. Maia, and P. Thibault, “Ptychographic wavefront characterization for single-particle imaging at x-ray lasers,” Optica **8**, 551–562 (2021).
36. P. Thibault and A. Menzel, “Reconstructing state mixtures from diffraction measurements,” Nature **494**, 68–71 (2013).
37. D. J. Batey, D. Claus, and J. M. Rodenburg, “Information multiplexing in ptychography,” Ultramicroscopy **138**, 13–21 (2014).
38. R. Röhrich, A. F. Koenderink, S. Witte, and L. Loetgering, “Spatial coherence control and analysis via micromirror-based mixed-state ptychography,” New J. Phys. **23**, 053016 (2021).
39. X. Zhang, A. R. Libertun, A. Paul, E. Gagnon, S. Backus, I. P. Christov, M. M. Murnane, H. C. Kapteyn, R. A. Bartels, Y. Liu, and D. T. Attwood, “Highly coherent light at 13 nm generated by use of quasi-phase-matched high-harmonic generation,” Opt. Lett. **29**, 1357–1359 (2004).
40. N. A. A. Aziz, E. Z. M. Tarmizi, and Y. Mansor, “Coherence measurement at different spatial points across high harmonic generation source using different spatial filter,” Macromol. Symp. **397**, 2000292 (2021).
41. S. Witte and K. S. E. Eikema, “Ultrafast optical parametric chirped-pulse amplification,” IEEE J. Sel. Top. Quantum Electron. **18**, 296–307 (2012).
42. L. Loetgering, T. Aidukas, M. Du, D. B. Flaes, D. Penagos, M. Rose, A. Pelekanidis, A. D. Beurs, W. Eschen, J. Hess, T. Wilhein, R. Heintzmann, J. Rothhardt, and S. Witte, “PtyLab: a cross-platform inverse modeling toolbox for conventional and Fourier ptychography,” in *OSA Imaging and Applied Optics Congress (3D, COSI, DH, ISA, pcAOP)* (Optica Publishing Group, 2021), paper CW6B.3.
43. T. Wodzinski, S. Künzel, J. C. P. Koliyadu, M. Hussain, B. Keitel, G. O. Williams, P. Zeitoun, E. Plönjes, and M. Fajardo, “High-harmonic generation wave front dependence on a driving infrared wave front,” Appl. Opt. **59**, 1363–1370 (2020).
44. R. J. Noll, “Zernike polynomials and atmospheric turbulence*,” J. Opt. Soc. Am. **66**, 207–211 (1976).